Int. J. Heat Mass Transfer. Vol. 33, No. 10, pp. 2295–2309, 1990
Printed in Great Britain

0017–9310/90 $3.00 + 0.00

Natural convection of opposing/assisting flows in vertical channels with asymmetrically discrete heated ribs

TSANG-YUAN LIN and SHOU-SHING HSIEH†

Department of Mechanical Engineering, National Sun Yat-Sen University, Kaohsiung, Taiwan 80424, Republic of China

(*Received* 21 *July* 1989 *and in final form* 28 *December* 1989)

Abstract—Both qualitative flow visualization as well as laser holographic interferometry and quantitative temperature measurement are presented for natural convection of air layers in vertical channels (channels A and B) with asymmetrically discrete heated ribs wherein the opposing flow is in channel A and the assisting flow is in channel B. Based on the analyses of the photographs and interferograms, it is suggested that the turbulent flow should be expected when the local modified Rayleigh number is in the range of 1.29×10^7–9.43×10^9 for both channels. The heat transfer data and flow visualization photographs indicate that the present rib geometry and the stratification are two major reasons influencing the temperature of the heated ribs. Average Nusselt number correlations are established in the form

$$\overline{Nu}_w = 0.12(Ra''_w)^{0.335}, \quad \overline{Nu}_w = 0.58(Ra''_w)^{0.201}, \quad 1.43 \times 10^5 < Ra''_w < 1.40 \times 10^6$$

for channels A and B, respectively. The power dependence strongly indicates that the flow in channel A is turbulent while the flow channel B is laminar.

1. INTRODUCTION

EFFECTIVE cooling of electronic components has become increasingly important as power dissipation and component density continue to increase substantially with the fast growth of electronic technology. In many electronic cooling situations, arrays of heat-dissipating components are mounted on flat-parallel plates forming a series of passages, each having either one very rough wall and the other relatively smooth or both walls rough. The simplest method of cooling these arrays is air circulated by naturally generated buoyant forces. Natural convection provides low-cost, reliable, maintenance-free, and electromagnetic interference-free cooling.

Studies on free convection from a discrete heat source on a vertical plate have been reported by Zinnes [1], and Carey and Mollendorf [2]. Park and Bergles [3] experimentally studied free convection from in-line and staggered arrays of heaters with varying distances between heaters. Moffat and Ortega [4] experimentally investigated the buoyant-induced convective heat transfer from an array of cubical elements that are deployed in an array on one wall of a vertical, open-ended parallel-plane channel. They reported that the heat transfer rate is significantly affected by the variation in the ratio of the gap width to the protrusion height of up to 4.

Kelleher *et al.* [5], Lee *et al.* [6], and Liu *et al.* [7] studied natural convection heat transfer in a rectangular enclosure with a heated protrusion on one vertical wall. The first two papers reported experimental (Part I) and numerical (Part II) studies of the geometric effects of a single two-dimensional heated protrusion mounted on one adiabatic wall of an enclosure. The opposing vertical wall is insulated while the top and bottom surfaces are isothermal. The experiments were conducted with water and the heat transfer and flow visualization results confirmed their numerical work. In the third paper, Liu *et al.* presented the results of a numerical study of three-dimensional convection cooling of an array of heated protrusions in an enclosure filled with a dielectric fluid. Recently, Keyhani *et al.* [8] reported an experimental study of natural convection in a vertical cavity with a discrete heat source. It was found that discrete flush-mounted heating in the enclosure results in local Nusselt numbers that are nearly the same as those reported for a wide flush-mounted heater on a vertical wall.

Although each pair of these vertical electronic card arrays have been investigated and modelled extensively as a buoyancy-driven flow in a differentially heated vertical cavity or channel depending on the end conditions extensively, most of these studies consider only one single channel (one passage). The buoyant fluid in the channel is either in an opposing or an assisting system. In view of the foregoing discussion and a detailed review of the literature, it indicates that, indeed, no effort has been made to study natural convection from double channels having two different flow directions with a flush-mounted heated pro-

† Author to whom correspondence should be addressed.

NOMENCLATURE

A_h surface area of the rib [m^2]
C isobaric specific heat [J kg^{-1} K^{-1}]
D depth of channel in the z-direction [m]
g acceleration due to gravity [m s^{-2}]
h local heat transfer coefficient, $Q_c/A_h(T_w - T_0)$
H height of the channel [m]
k thermal conductivity [W m^{-1} K^{-1}]
L length of the channel, $2H$ [m]
L_1 surface length of the heated rib [m]
L_2 length of the gap between a pair of heated ribs [m]
Nu Nusselt number, h[length scale]$/k$
Pr Prandtl number, ν/α
Q power input per heated rib [W]
Q_c convective heat transfer rate [W]
Q_L conduction heat loss [W]
Q_r radiation heat loss [W]
Q_{sc} substrate conduction heat transfer rate [W]
Q_t total power input to each test rib [W]
Ra Rayleigh number, $g\beta(T_w - T_0)$ [length scale]$^3/\nu\alpha$
Ra^* modified Rayleigh number, $Nu\ Ra$
Ra'' modified channel Rayleigh number, $Ra^*(W/H)$
T temperature [°C]
T_f reference fluid temperature, $0.5(T_w + T_0)$ [°C]
T_0 inlet temperature of air [°C]
T_w local temperature of the heated rib [°C]
W width of the channel [m]
x, y, z Cartesian coordinates [m].

Greek symbols
α thermal diffusivity, $k/\rho C$ [m^2 s^{-1}]
β volume coefficient of expansion [K^{-1}]
ν kinematic viscosity
ρ density [kg m^{-3}]
σ standard deviation.

Subscripts
W channel width
y local height, measured from top of channel A/bottom of channel B to mid-height of heated rib.

Superscript
$\bar{}$ average value.

trusion on each channel wall. It is believed that a substantial body of experimental data is needed in order to have a complete description of heat transfer, flow field, and flow regime in this important area of electronic packaging problems.

The purpose of the present work is to extend the previous studies of the buoyancy-driven flow and heat transfer in a single vertical cavity or channel with discrete heated protrusions on one vertical wall to double vertical channels with two different flow systems (opposing/assisting).

2. EXPERIMENTAL APPARATUS AND PROCEDURE

The experimental apparatus consists of double channels with eight alternately unheated and flush-mounted rows of isoflux heated ribs on each channel wall with $H/W = 16$, $D/W = 20$, $L_1/W = 0.51$, $L_2/W = 1.47$, and $W = 50$ mm. The geometry, coordinate system, boundary conditions, and the details of the experimental apparatus are given in Fig. 1. The data that will be presented are for air ($Pr \sim 0.7$) with an approximate power input $Q = 5$, 10, 20, 35, and 48 W per rib. The heated rib wall of the test cell, 800 × 1000 mm, was constructed out of 10 mm thick aluminium sheet ($k = 177$ W m^{-1} K^{-1}). Sixteen two-dimensional aluminum ($k = 186$ W m^{-1} K^{-1}) ribs, 25.4 mm wide, 25.4 mm deep, and 1000 mm long, were adhered to the plate. Sixteen slots, 22.2 mm wide, 22.2 mm deep, and 1000 mm long were cut in these ribs in order to place 0.4 mm cartridge heaters with an outer diameter of 7.4 mm into a 1.3 mm quartz-made shield. The experiments reported in this paper were conducted with 16 heated ribs, eight on each channel. Each heater was covered with 1.6 mm thick aluminum plate with a heat sink compound (MgO) filled between the heater and the aluminum strip to reduce contact resistance. Thermocouples were then placed in grooves that were milled into each of the heated ribs and unheated sections of the wall. These thermocouples were located at their respective sections shown in Fig. 2. All the thermocouples used in the instrumentation were 28 gauge copper–constantan type.

Thermocouples were also placed at different depths in the plexiglass or aluminum plate to estimate the conduction loss. Heater leads and thermocouple wires were taken out through the holes made in plexiglass/aluminum plate, and were connected to a power panel and a digital data acquisition system, respectively. The power panel consisted of a voltage stabilizer, and a step-down transformer. Voltage information for each heated rib was fed to the data acquisition system coupled with a personal computer for data reduction and analysis.

All the other sides of the channels were made out of plexiglass, 10 mm thick and of length $L = 1600$

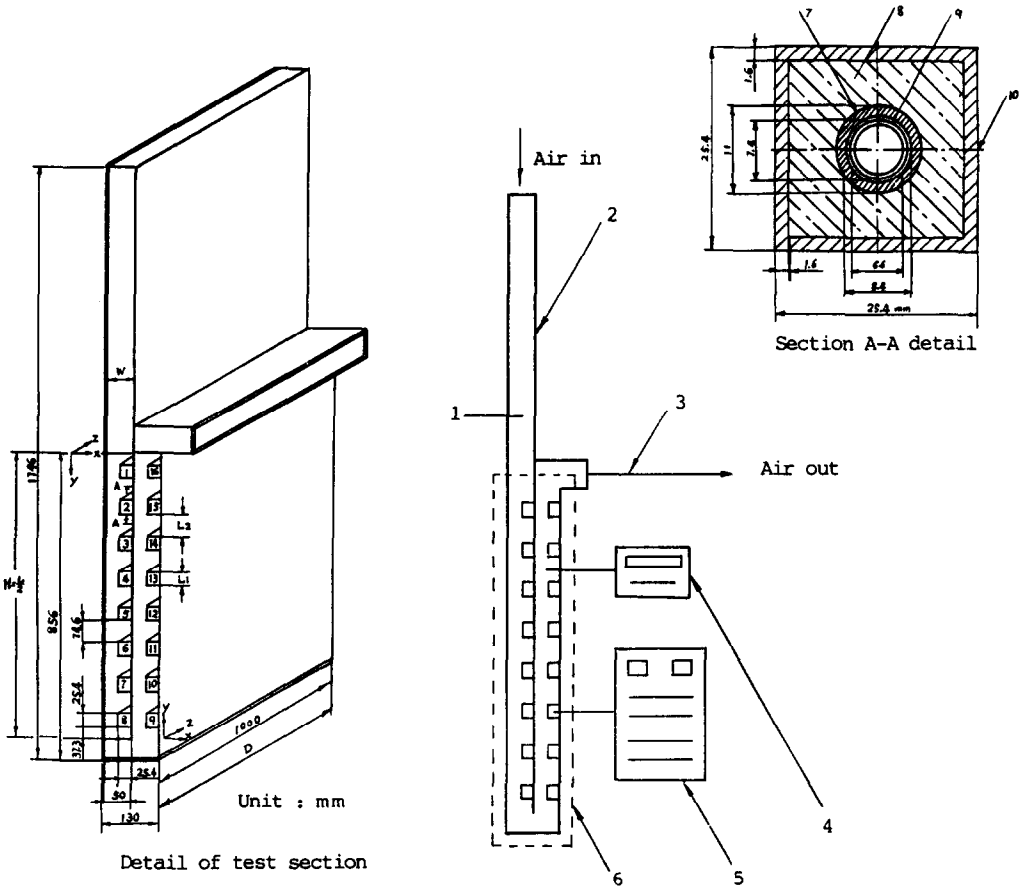

FIG. 1. Schematic of experimental apparatus: 1, hot wire anemometer; 2, plexiglass channel; 3, aluminum duct; 4, data acquisition system; 5, power input controller; 6, test section; 7, quartz tube; 8, MgO compound; 9, cartridge heater; 10, aluminum rib.

mm. To form the channel, holes were drilled at all four corners of each plate and then bolted together. Channel spacing was maintained and resulted in an aspect ratio of 20 for the cross sectional area in which the flow is perpendicular to it. The power in each heater could be up to approximately 48 W, i.e. 486.1 W m^{-2} for the heated sections. The conduction losses through various walls of the channels were also calculated to obtain net energy transported by the convective fluid. In general, the conduction loss was within 4.87% of the total input for the present experiments.

To examine the flow structure, flow visualization experiments were conducted for several power inputs. The smoke generation method was applied with a CCl_4+TiCl_4 mixture (mixing ratio 1 : 10) and air as the convection medium to visualize the flow. The illumination of the smoke was done by using a slide projector as a light source shining through a narrow slit so as to produce a plane of light. All photographs were taken with a Cannon-T90 camera on Konica SR-V 3200 film with exposure times of 1/8–1/15 s.

In addition to temperature measurement using thermocouples, both channels were placed in the test beam of a laser holographic interferometer for further understanding of the thermal characteristics of the study. The laser holographic interferometry used in this study is essentially the same as that described by Aung and O'Regan [9] and is shown schematically in Fig. 3. Coherent light (0.6328 μm), from a 35 mW Spectra-Physics model 124-B He–Ne laser is split into an object beam and a reference beam by a variable silvered mirror and each beam is expanded to a 90 mm planar wave via a 20 × microscopic objective and a 60 × microscopic objective and two collimating lens (diameter 12.7 cm). Pinholes of 20 μm diameter are located at the focal points of the microscopic objectives in order to eliminate intensity variations in the wave fronts. The two wave fronts intersect at the photographic plate (here at an angle of 30 deg) and produce a hologram when the photographic emulsion is exposed simultaneously to the two beams and then developed *in situ*. The interferometer components and test section are mounted securely to a 1.4 × 2.0 m vibration-free optical table.

3. UNCERTAINTY ANALYSIS

A Solartron 3530 Orion automatic data acquisition system was used for data collection. The thermo-

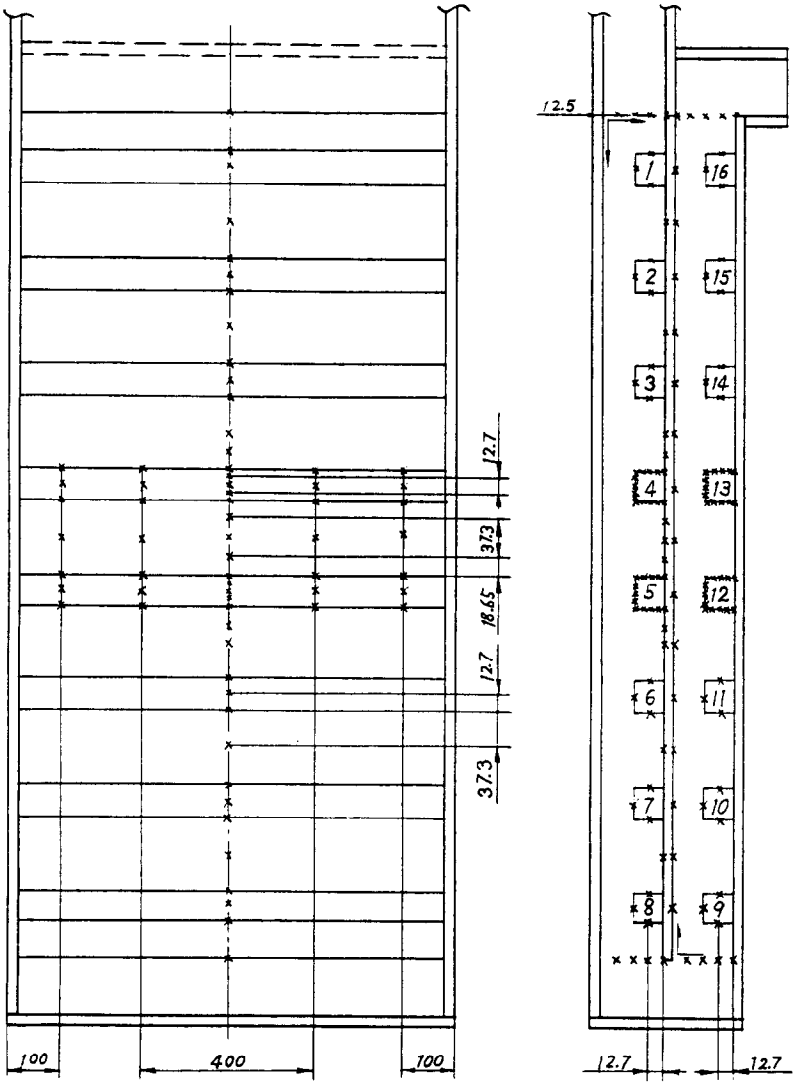

FIG. 2. Detailed thermocouple position for temperature measurement.

couple outputs were measured to ± 1 μV, which results in ± 0.01°C sensitivity. A conservative estimate of the accuracy of the temperature measurement is ± 0.1°C. The voltage input to each heater circuit was measured with a sensitivity of ± 1 mV and an accuracy of $\pm 0.1\%$. Several runs were conducted where the voltage and the current for the circuit were measured, and the calculated resistance was highly stable. These data indicated a maximum uncertainty of $\pm 1\%$ in the resistance of the circuit. The power input to the circuit was then calculated by using the measured voltage drop across the circuit and its respective resistance. This procedure resulted in a maximum uncertainty of $\pm 2\%$ in the calculated power inputs. The uncertainty associated with the length scale used in the data reduction was ± 1 mm. The thermophysical properties of the air were assigned an uncertainty of $\pm 3\%$. Their judgement was based on the observed variations in the reported values in the literature.

The overall uncertainty in the Nusselt and Rayleigh numbers varied with the power input. Smaller power input results in a larger uncertainty primarily because of a lower temperature difference across the channel and a higher fraction of energy lost by conduction. As the power input is increased, the uncertainty in the experimental data decreases. The estimated uncertainties in Nu and Ra are 1.6–5.8, and 1.0–5.4%, respectively. It should be noted that the uncertainty in these parameters is reduced when they are considered in terms of local values since the percentage error in the length measurement is decreased.

4. DATA REDUCTION

The local values of the thermophysical properties of air were obtained at a reference fluid temperature of

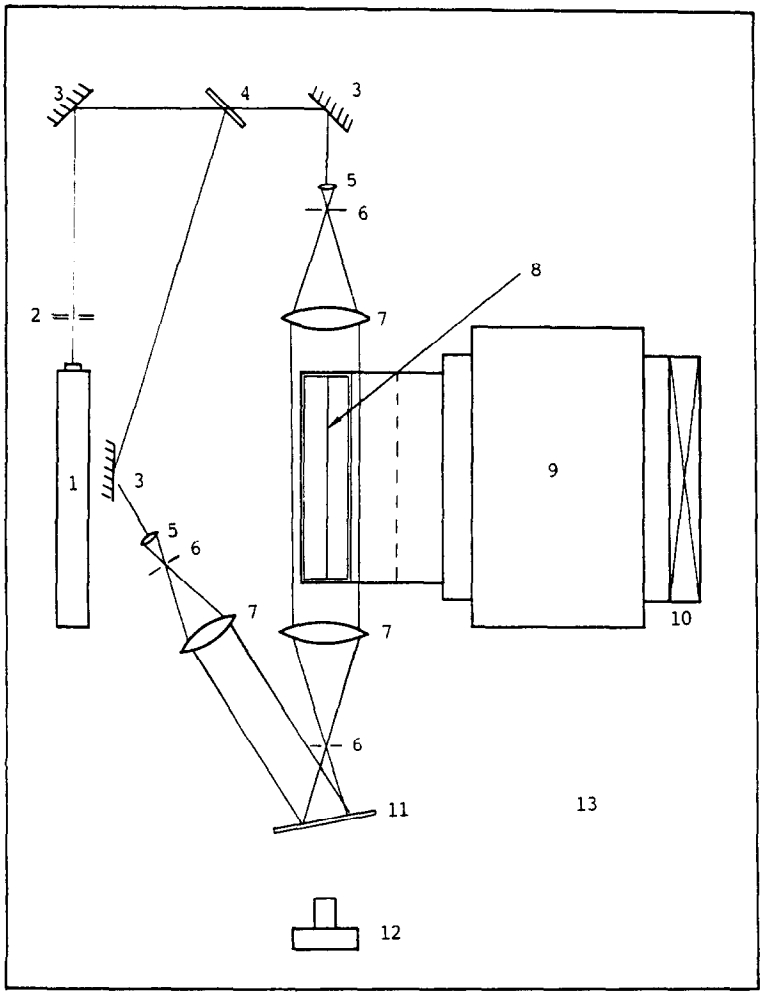

FIG. 3. Schematic of holographic interferometer for thermal field: 1, helium–neon laser; 2, shutter; 3, mirror; 4, beam splitter; 5, objective lens; 6, pinhole; 7, collimating lens; 8, test section; 9, duct; 10, fan; 11, holographic plate; 12, camera; 13, vibration-free optical table.

$$T_f = 0.5(T_w + T_0)$$

where T_w is the local temperature of the heated segment, and T_0 the inlet temperature of air. The net convective heat flow rate, Q_c, from the test surface to the air in the test channel, was calculated based on the following energy balance equation:

$$Q_c = Q_t - Q_L - Q_{sc} - Q_r \quad (1)$$

where Q_t is the total power input to each test rib, Q_L the conduction heat loss from the ends of the heater to the laboratory environment, Q_{sc} the substrate conduction heat transfer, and Q_r the radiative heat loss from the rib surface to its surroundings. The substrate conduction heat transfer, of which it eventually is convected to the working fluid in the unheated section, was calculated using a two-dimensional unit cell finite-difference conduction model. The value of Q_r was evaluated using a diffuse gray-surface network [10]. The radiant heat exchanges among all the side walls. The maximum radiative heat loss is less than 4.31% of the total power input for all the cases investigated.

After Q_L, Q_{sc}, and Q_r were estimated, the net convective heat flow rate, Q_c, from the rib surface can be obtained. Therefore, the local heat transfer coefficients, Nusselt, Rayleigh, and modified Rayleigh numbers used in the presentation of the data were calculated from

$$h = Q_c/A_h(T_w - T_0) \quad (2)$$

where A_h is the surface area of the rib and $(T_w - T_0)$ the temperature difference between the rib and the inlet air temperature

$$Nu = h[\text{length scale}]/k \quad (3)$$

$$Ra = g\beta(T_w - T_0)[\text{length scale}]^3/\nu\alpha \quad (4)$$

$$Ra^* = Nu\ Ra \quad (5)$$

$$Ra'' = Ra^*(W/H). \quad (6)$$

Two length scales of local height y (Nu_y, Ra_y, Ra_y^*), and channel width W (Nu_W, Ra_W, Ra_W^*, Ra''), are used, where appropriate, in the presentation and discussion of the results.

Table 1. Average Rayleigh and Nusselt numbers for experiments of air layers ($L_3/L_1 = 2.90$, $L_2/W = 1.47$, $0.69 < Pr < 0.71$)

Run No.	Q (W)	Ra_W^*	Ra_W''	$\overline{Ra}_W$	$\overline{Nu}_W$ Channel A	$\overline{Nu}_W$ Channel B
1	5	1.14×10^6	1.43×10^5	1.80×10^5	6.28	6.25
2	10	2.52×10^6	3.16×10^5	3.09×10^5	8.26	7.62
3	20	4.69×10^6	5.86×10^5	4.77×10^5	10.45	8.50
4	35	8.10×10^6	1.01×10^6	7.12×10^5	12.04	9.39
5	48	1.12×10^7	1.40×10^6	8.88×10^5	13.50	9.96

5. RESULTS AND DISCUSSION

The present study was approximately conducted for $Q = 5$, 10, 20, 35, and 48 W per heating element with atmospheric air as the convective medium. This covered a Rayleigh number range of $\overline{Ra}_W = 1.80 \times 10^5$–$8.88 \times 10^5$ while the local Prandtl number varied between 0.69 and 0.71. The range of average modified Rayleigh number Ra_W^* studied in these experiments was 1.14×10^6–1.12×10^7 which can be seen from Table 1.

5.1. *Flow visualization*

The present results mainly focus on the local steady-state behavior. To assist in explaining the local flow structure, flow visualization was made through a smoke generator under the steady-state condition. The steady-state condition was determined when the variation of temperature of the rib was less than 1% of that of its previous value. It usually takes 4–5 h to reach a steady state. In order to bring a better understanding of the results and discussion, a schematic of the physical system with major flow structure of the present study is shown in Fig. 4. We designate the channels as channel A (the left channel) and channel B (the right channel). The optical lens used in the present laser-interferometry system is small so that it only consists of eight ribs. The typical flow patterns visualized in the central portion of both channels are demonstrated in Figs. 5(a)–(c), for three different Rayleigh numbers, respectively. At $Ra_W^* = 1.90 \times 10^5$, Fig. 5(a) basically shows a cell within two consecutive ribs for channel A, which indicates a buoyancy driven fluid flow within two consecutive ribs. However, the main flow adjacent to the cold wall moves downward which causes the major part of the fluid motion to take place at the cell and that accounts for the majority of the convective heat transfer.

For a definite rib position, in channel A, the location of the cell separation shear layer is dependent on the Rayleigh number. As the Rayleigh number increases, the location of the separation layer changes dramatically which can be seen from Figs. 5(b) and (c). This separation layer is located very near the upstream front corner of the rib shown in Figs. 5(a) and (b). However, in Fig. 5(c), it is found that this separation layer does not touch the rib wall. The flow of the buoyancy driven cell follows the present geometry. The fluid rises from the vertical face of the rib, over the upstream front face of the rib and then up the vertical wall of the valley of the two consecutive ribs to which the next rib is attached. Inertia then carries the fluid across the cold surface of the main flow and then down the vertical wall opposite the rib. This phenomenon becomes more distinct as Rayleigh number increases until the cell may not have enough energy to maintain its recirculating motion. This is because the velocity of the downward main flow is so fast that the initial slow motion in the cell at low Rayleigh number was unable to keep its original path, i.e. the cell was eventually broken down and it no longer exists at a Rayleigh number of 2.09×10^6.

Channel B has a totally different flow structure due to the different boundary conditions. The cold wall was at a lower temperature for channel A while the temperature of the cold wall for channel B starts simultaneously to rise up through substrate conduction because of the heating element of channel A. Moreover, the main flow moves upward which has the same direction as the flow due to the buoyancy effect. Based on these two different conditions, it is not possible to expect that there exists the same flow structure in these two channels. Actually, one is opposing flow, one is assisting flow. The thermal boundary layer becomes thicker as the upward main flow moves further downstream in channel B and the wall plume-like behavior near the channel wall develops. Figures 5(a)–(c) show that the plume almost occupies the entire channel width and interacts with the fluid trapped in the valley of two consecutive ribs as the Rayleigh number increased to $Ra_W^* = 2.09 \times 10^6$. It is interesting to note that it is possible to have laminar and turbulent flow coexist across both channels (Fig. 5(b)). The flow pattern above the midheight region of the channels at $Ra_W^* = 2.09 \times 10^6$ shows that the flow along the 'hot' walls goes through a transition from laminar to turbulent flow for both channel 'hot' walls, while the downward flow in channel A along the cold wall is clearly laminar even at $Ra_W^* = 2.09 \times 10^6$.

In order to determine the value of the critical local Rayleigh number for the onset of turbulent flow, Figs. 5(a)–(c) showing the details of the flow above the midheight of the channel, have been analyzed. The results of the analysis of the photographs are tabulated in Table 2. In that table, the lowest Ra_y and Ra_y^*

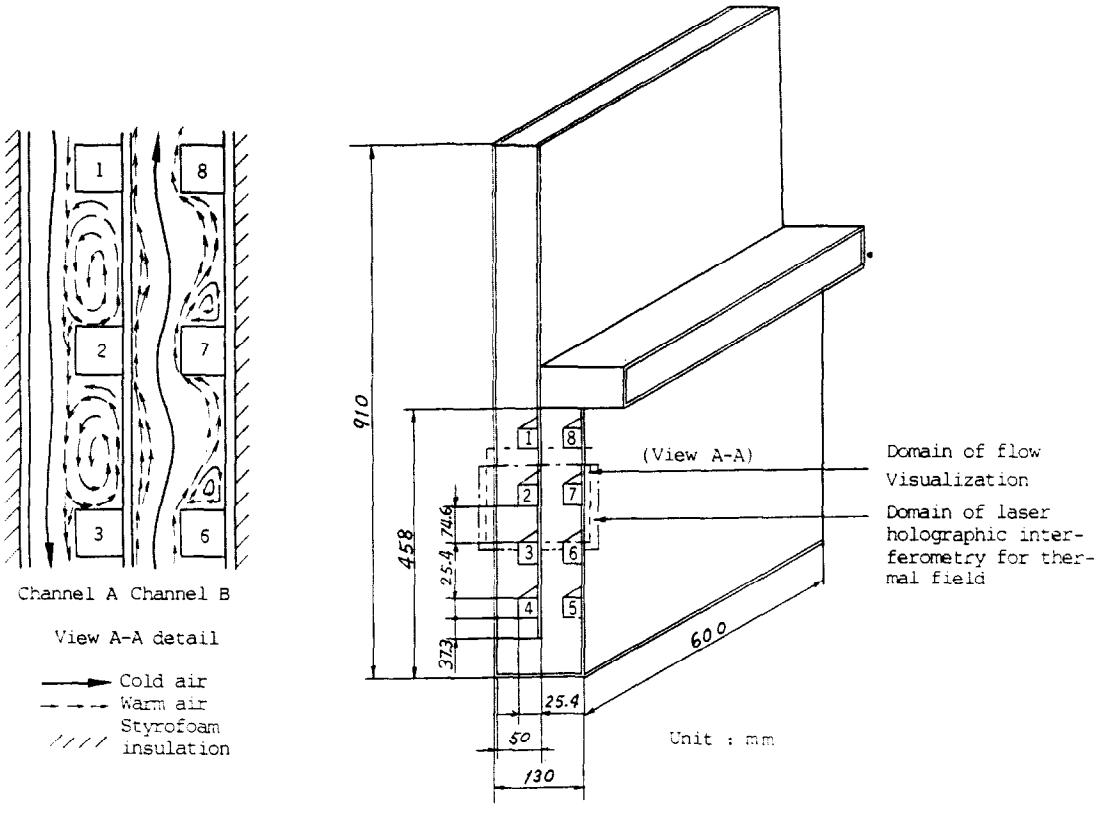

FIG. 4. Domain of flow/thermal fields by optical visualization.

at which unsteady or turbulent flow was first observed, as well as the maximum Ra_y and Ra_y^* at which the flow was laminar are given. The data in Table 2 clearly indicate that the modified Rayleigh number is the appropriate parameter for specifying the critical value for onset of turbulence. Based on these data, and allowing for one L_1 error in specifying the local height, it is suggested that turbulent flow would be expected when $1.29 \times 10^7 < Ra_y^* < 9.43 \times 10^9$.

In general, the present flow patterns are similar to those observed by Kelleher *et al.* [5] and other investigators studying forced convection in horizontal channels/ducts with asymmetrically heated ribs. However, no statement can be made with respect to differences in the velocities, or for that matter, the sequence of change in flow pattern with respect to a common flow parameter.

5.2. *Qualitative description of the temperature field*

Figures 6 and 7 show interferograms of the temperature field in both channels in the infinite fringe mode for two different cases. The resulting fringes are then isotherms. Figure 6 shows the temperature contours near the ribs while Fig. 7 shows the isotherms for the valley between two consecutive ribs.

A closeup view of the air-filled channels at $Ra_H^* = 1.14 \times 10^6$ is shown in the interferograms in Figs. 6 and 7 for two locations, respectively. The measured isotherm patterns in Fig. 6 indicate that the surface heat flux is reduced along the wall just below and just above the element compared with what it would be on a smooth wall. The temperature gradient at the outer surface of the element appears to be high, especially near the upper (for channel B)/lower (for channel A), outside corner. This characteristic is similar to that reported by Shakerin *et al.* [11] investigating natural convection in an enclosure with discrete roughness elements on a vertical heated wall. Furthermore, the present isotherm patterns along the 'cold' wall for both channels coincided with the previous findings of the flow patterns because they show that the thermal boundary layers do interact as evidenced by the thermal stratification along the cold wall in channel A and the wall plume development of the cold wall in channel B. In Fig. 7, the measured isotherm patterns for both channels in the valley of two consecutive ribs have the same trend at $Ra_H^* = 1.14 \times 10^6$ except outside the cavity which is due to the different flow types (one for opposing flow; one for assisting flow). The temperature gradient along the vertical wall of the channel appears to be higher for channel A than that for channel B.

Further qualitative information about the nature of the temperature distribution was obtained. In general, provided there is no change in the direction of fluid motion, the width of a fringe will remain constant along its path. When fringes become thinner and get closer to each other, this implies a region of high heat

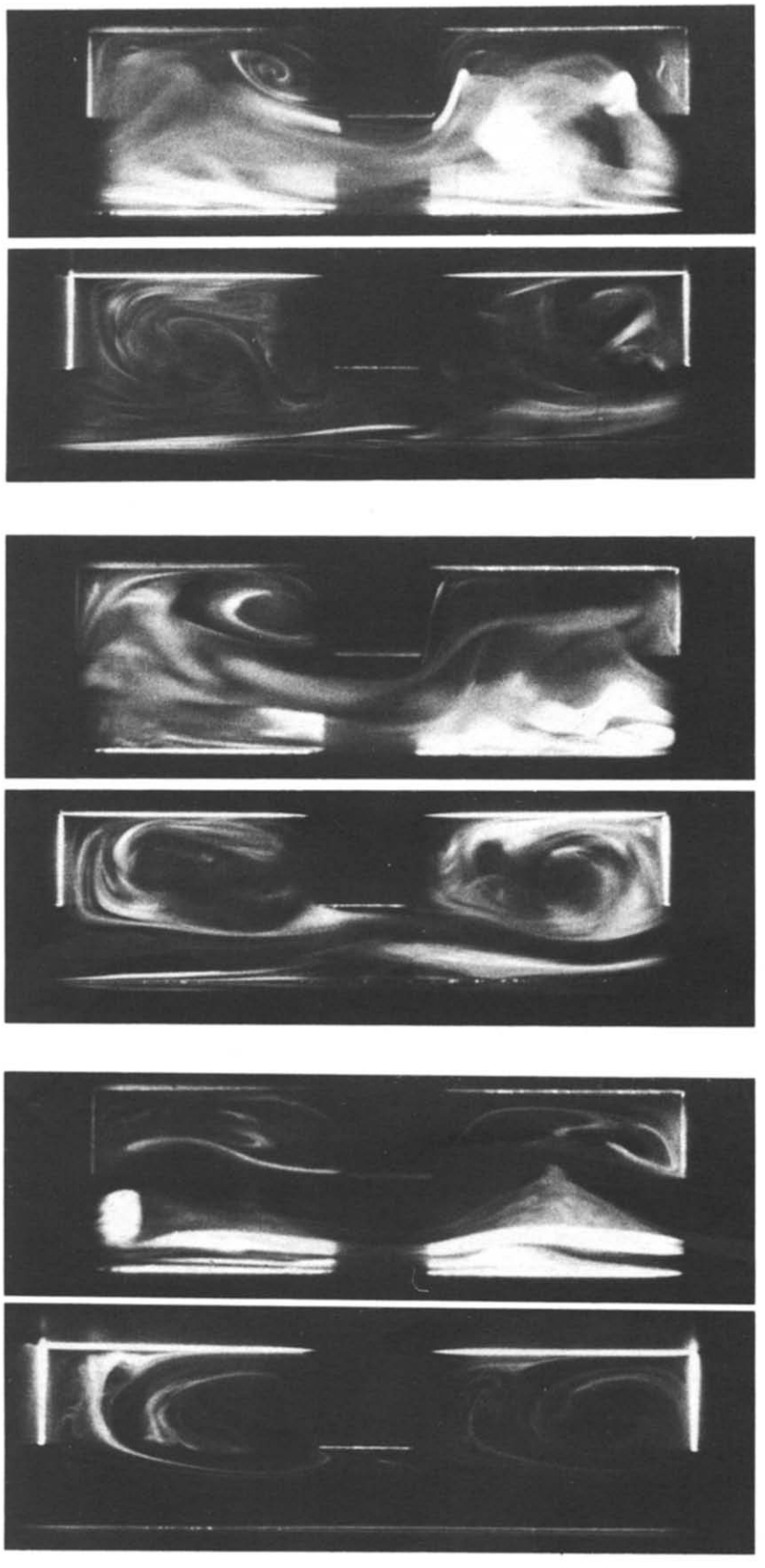

FIG. 5. Photographs made by flow visualization: (a) $Ra_H^* = 1.90 \times 10^5$; (b) $Ra_H^* = 2.09 \times 10^6$; (c) $Ra_H^* = 7.36 \times 10^6$.

Table 2. Lowest local Rayleigh numbers (Ra_x, Ra_y^*) at which unsteady or turbulent flow was observed

			Observed flow condition			
			Laminar	Unsteady or turbulent	Laminar	Unsteady or turbulent
Q (W)	Channel	Rib No.	Ra_x		Ra_y^*	
1	A	1	9.34×10^4		4.57×10^5	
		2	1.03×10^6		1.05×10^7	
		2	1.75×10^6		2.07×10^7	
		3	5.33×10^6		9.35×10^7	
	B	6	1.73×10^6		2.07×10^7	
		7	5.40×10^6		9.35×10^7	
		7	7.10×10^6		1.41×10^8	
		8	1.56×10^7		3.82×10^8	
10	A	1	3.88×10^5		4.52×10^6	
		2	4.52×10^6		1.02×10^8	
		2		7.73×10^6		2.01×10^8
		3		2.34×10^7		9.13×10^8
	B	6	8.80×10^6		1.96×10^8	
		7	2.73×10^7		8.88×10^8	
		7		3.59×10^7		1.34×10^9
		8		7.61×10^7		3.65×10^9
30	A	1		8.80×10^5		1.29×10^7
		2		9.96×10^6		2.86×10^8
		2		1.68×10^7		5.59×10^8
		3		5.13×10^7		2.55×10^9
	B	6		2.02×10^7		4.92×10^8
		7		6.27×10^7		2.23×10^9
		7		8.30×10^7		3.41×10^9
		8		1.72×10^8		9.43×10^9

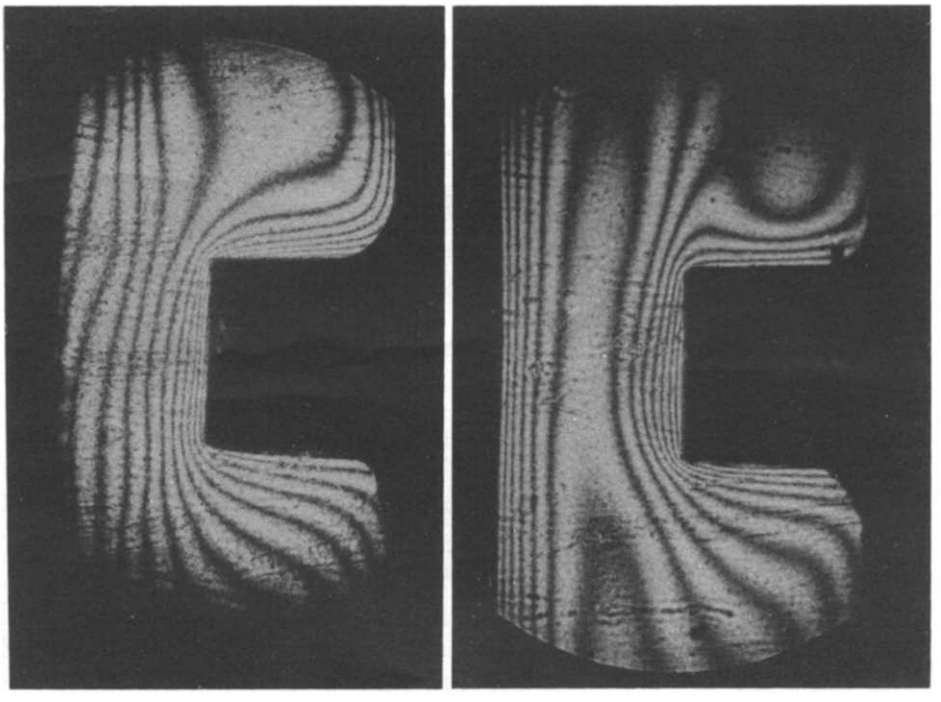

FIG. 6. Interferograms for the flow near the vicinity of the rib at $Ra_H^* = 1.14 \times 10^6$ (ribs 2 and 7).

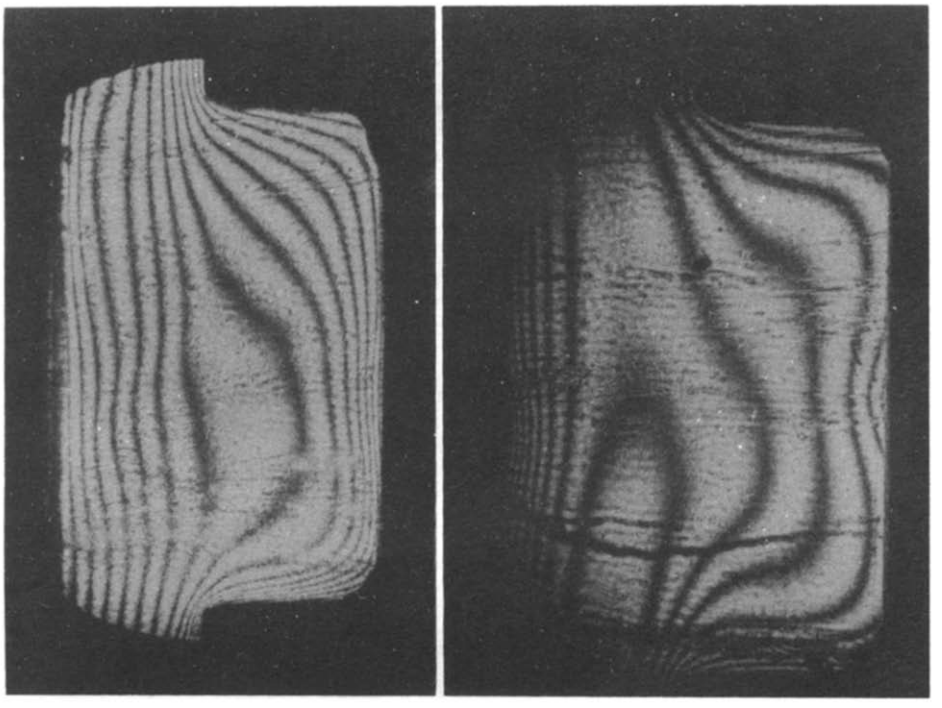

FIG. 7. Interferograms for the flow near the valley of two consecutive ribs at $Ra_H^* = 1.14 \times 10^7$ (between ribs 2 and 3, and 6 and 7).

transfer which can be seen from Fig. 6 for the flow along the vertical rib wall in channel B or A. The fringe closest to the wall in the natural convection region remains unchanged in direction but increases in thickness as it approaches the side walls. The higher order fringes possess high curvature due to flow separation/recirculation. There is, however, an instability present which can be noticed in Fig. 6 by the thicker arc-shaped isotherms for the flow near the upper/or lower portion of the ribs. These two characteristics can also be applied to Fig. 7 to depict the present observations. Along the vertical walls of the cavity, the fringes are thinner and followed the contour of the cavity. However, away from the wall, due to the recirculation-like flow, arc-shaped isotherms happen elsewhere near the center of the recirculation. The fringe was thickened the most. Incidentally, wall plume-like behavior near the core flow in channel B for Fig. 6 is clearly noted. This also verifies the previous findings based on the flow visualization. Since the image processing system is not available to the authors at this stage, it is not possible to get quantitative information from the present interferograms.

5.3. *Temperature distribution*

The temperature distribution, $T_w - T_0$, along the streamwise direction at each rib for both channels for $1.14 \times 10^6 < Ra_H^* < 1.12 \times 10^7$ is given in Fig. 8. Each rib has three thermocouple measurement positions. They are located at the top floor, front and rear face of the rib, respectively.

The temperature of the heated unheated sections shows a steady increase from heated rib 1 to heated rib 16. However, a near constant temperature distribution was found for lower Rayleigh numbers ($Ra_H^* < 1.14 \times 10^6$). A slight temperature inversion at $0.4 < y/H < 0.5$ for channel B is observed. This phenomenon persists for larger Rayleigh numbers, for instance, $Ra_H^* = 1.12 \times 10^7$. This behavior has also been reported in the boundary layer regime in the vertical cavity with isothermal heated smooth wall without protrusion by Choi and Korpela [12] and other investigators. The variation of wall (both heated unheated) temperature depends on changes in the flow pattern (e.g. flow separation/recirculation), flow type (opposing/assisting flow), flow regime (e.g. laminar, transitional, unsteady, and turbulent) and the stratification parameter (e.g. channel height H and slope of the temperature variation near the wall). Therefore, no single explanation can be drawn at this stage for the measured profiles. The convection heat transfer is dependent on the temperature gradient near the surface, which in turn is strongly influenced by the stratification parameter and the flow structure (presence of separation/recirculation). In order to illustrate the effect of stratification on the surface temperature distribution, for both channels, $T_w - T$ is nearly constant for all heated ribs (except ribs 1, 8, 9, and 16), for $Ra_H^* < 2.52 \times 10^6$ as stated earlier. The two cases correspond to flow conditions where the laminar flow regime covers a large vertical extent of the channels. As mentioned before, as Rayleigh num-

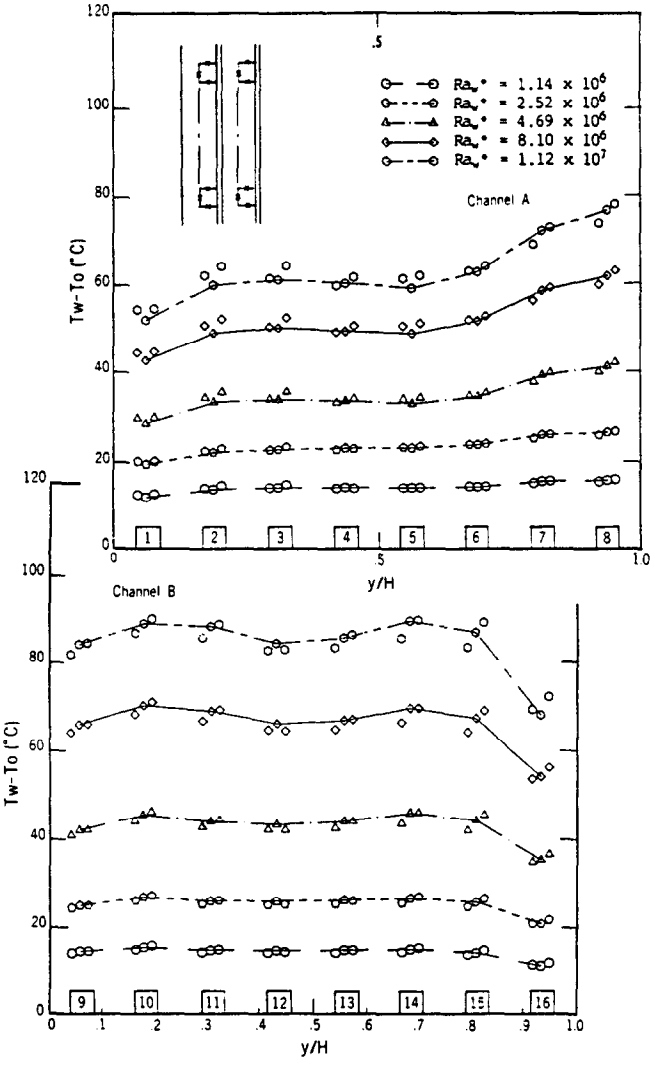

FIG. 8. Streamwise temperature distribution along the rib wall.

ber increases, the portion of the channel which covers the laminar regime decreases. The disappearance of the laminar flow regime was observed at $Ra_w^* = 7.36 \times 10^6$ for both channels. The data in Fig. 8 indicate that $T_w - T_0$ for ribs 2–7 and 9–15 can be approximated with an average value of 13.9% for $Ra_w^* < 8.10 \times 10^6$. The temperature differences for $Ra_w^* = 2.09 \times 10^6$–$1.12 \times 10^7$ correspond to flow regimes where the transitional, unsteady or turbulent flow prevails. Indeed, for $Ra_w^* = 4.69 \times 10^6$, $T_w - T_0$ of ribs 1 (turbulent-like flow) and 16 (laminar-like flow) are 11.7°C (33.3%) and 6.3°C (14.3%) less than that of ribs 8 (turbulent-like flow) and 9 (laminar-like flow), respectively, for the corresponding channels. Furthermore, it is expected that, due to the present rib geometry, separation, with reverse flow at the wall or at the surface of the rib was observed in the experiments. In fact, unsteady flow reversal and shedding from the rib were noticed for $Ra_w^* > 2.09 \times 10^6$. This highly unstable, separated shear layer created in the flow over repeated ribs undergoes rapid transition to turbulence when compared with the wall without ribs, and may augment heat transfer. This will be verified later in the upcoming discussion.

5.4. *Heat transfer results*

Figure 9 presents the local Nusselt number Nu_w plotted against streamwise downstream distance. Figure 9 shows that for a fixed power input (or Ra_w^*), the heat transfer coefficient generally decreases with an increase in distance in the downstream direction in channel A while the heat transfer coefficient in channel B increases with an increase in distance. The variation in Nu_w is minimal between the pairs of ribs 2 and 3, 4 and 5, 10 and 11, and 14 and 15, whereas it is largest between ribs 1 and 2, 6 and 7, 9 and 10, and 15 and 16. It is possible that the heat transfer coefficient for rib 4 exceeds that of rib 3. It should be pointed out that those heat transfer coefficients are calculated based on the temperature difference of $T_w - T_0$. Therefore, the

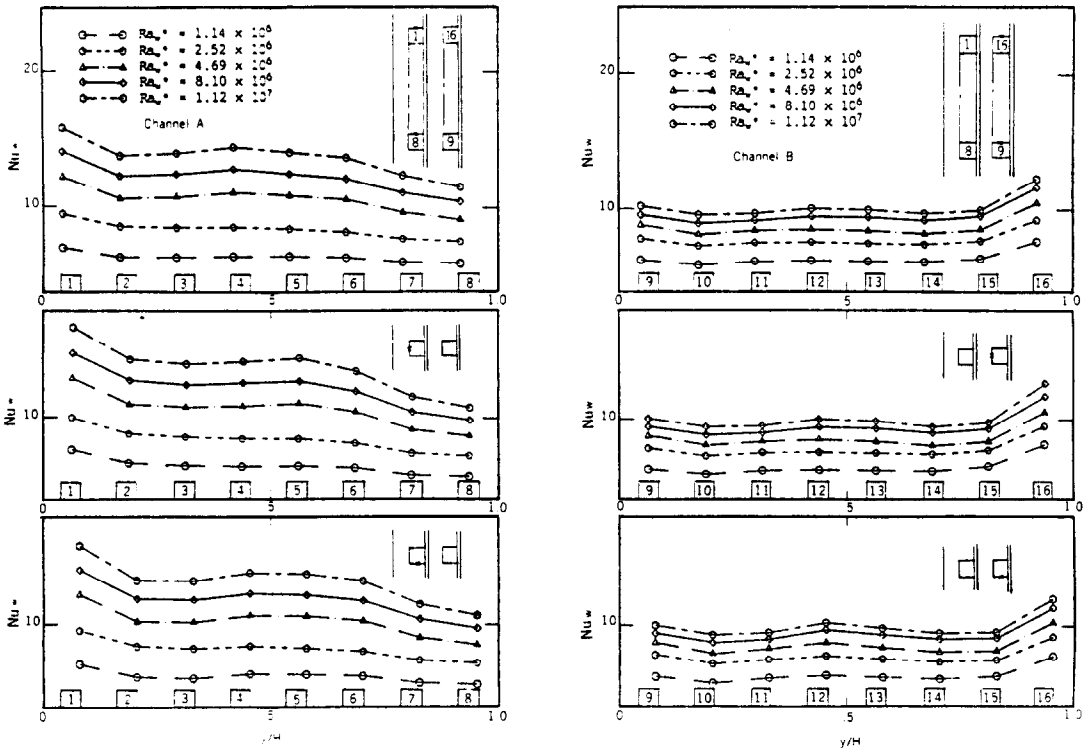

FIG. 9. Local Nusselt number vs downstream distance.

difference among the Nu_w of the ribs are partially due to stratification. Nevertheless, the change in the flow pattern and flow regime can be of sufficient impact to override the stratification effect, this resulting in a slightly higher Nu for rib 4 than for rib 3. Park and Bergles [3] have reported that the ratio of the heat transfer coefficient of the top heater to that of the bottom one for the case of two flush in-line heaters at a fixed modified Rayleigh number reduces from an asymptotic value of 0.9 to 0.78 as L_2/L_1 decreases from 9.94 to 1.42. For the present study ($L_2/L_1 = 2.94$), the ratios of the heat transfer coefficient of rib 2 to that of rib 1 for channel A and of rib 10 to that of rib 9 for channel B, at a fixed Ra_w^*, are 0.85 and 0.90, respectively. The Nu_w of each heated rib is correlated in terms of Ra in the form

$$Nu_w = C(Ra_w^*)^m. \quad (7)$$

Constants C, exponents m, and the standard deviation σ, are tabulated in Table 3. These correlations represent the experimental data with a maximum error of 3.7%.

The relationships between Nu_y and Ra_y^* for the cases under study are shown in Fig. 10. The correlations for all the ribs in both channels A and B have been correlated in terms of Ra_y^* as

$$Nu_y = 0.32(Ra_y^*)^{0.235}, \quad 3.21\times10^5 < Ra_y^* < 3.46\times10^{11} \quad (8)$$

$$Nu_y = 0.17(Ra_y^*)^{0.257}, \quad 3.16\times10^5 < Ra_y^* < 3.69\times10^{11}. \quad (9)$$

The present values of Nu_y are compared with the predicted/measured Nusselt number for a smooth vertical plate for constant heat flux reported by Vliet [13] also shown in Fig. 10. The data was correlated as

$$Nu_y = 0.6(Ra_y^*)^{0.2} \quad (10)$$

Table 3. Coefficients C, exponents m, and deviation σ, for heat transfer correlation (equation (7))

Rib No.	C	m	σ
1	0.065	0.340	0.034
2	0.069	0.326	0.029
3	0.062	0.333	0.037
4	0.056	0.340	0.012
5	0.058	0.338	0.018
6	0.067	0.327	0.025
7	0.089	0.301	0.017
8	0.125	0.276	0.026
9	0.385	0.201	0.036
10	0.356	0.201	0.026
11	0.464	0.186	0.029
12	0.365	0.204	0.022
13	0.380	0.200	0.020
14	0.440	0.189	0.026
15	0.520	0.180	0.022
16	0.532	0.192	0.007

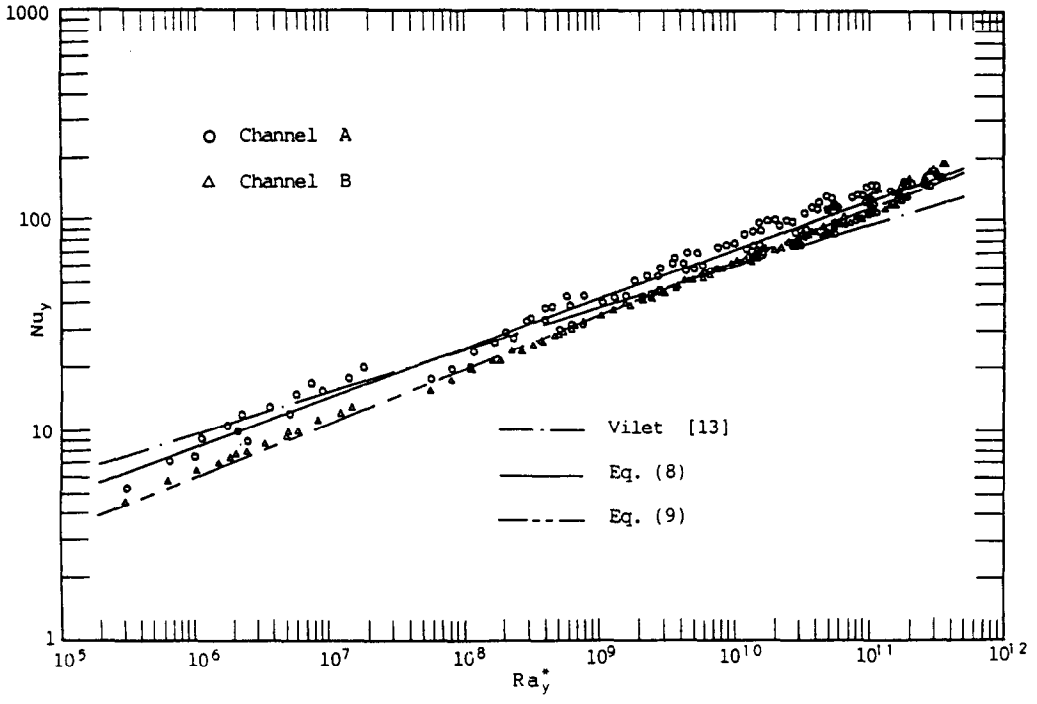

FIG. 10. The relationship between Nu_y and Ra_y^*.

predicted Nusselt numbers from 0.3 to 20.3% higher than the present results for both channels for $Ra_y^* < 6.3 \times 10^7$. However, for $Ra_y^* > 6.3 \times 10^7$, the present result for channel A predicted Nusselt numbers from 1.0 to 35.2% higher than that obtained by Vliet [13].

At this stage, it may be interesting to compare the present heat transfer results with those for a vertical channel fully heated on one side wall. Figure 11 presents the results that the heat transfer characteristics in the upstream region of channel A are of the turbulent-flow type while those in the downstream region of channel B are of a laminar-flow type. It can be verified that the slope of the curve in Fig. 11 in each region equals about 1/3 in the upstream region and 1/5 in the downstream region. This confirms the previous findings (see Section 5.1) to a great degree. The correlation predicts the experimental data with an average error of 1.6%. The minimum and maximum errors are 0.1 and 3.1%, respectively. The experimental data of Wirtz and Stutzman [14], presented in Fig. 11 were conducted for natural convection between vertical plates with symmetric heating. The comparison made for $\overline{Nu}_W$ plotted against Ra_W'' indicates that the present data for channel B coincides with that of Wirtz and Stutzman. While, for channel A, the values of $\overline{Nu}_W$ are compared with measured Nusselt numbers obtained by Bar-Cohen and Rohsenow [15]. It is found that the present study predicted Nusselt numbers from 4.9 to 28.2% higher than that of Bar-Cohen and Rohsenow for $Ra_W'' > 2.2 \times 10^5$.

6. CONCLUSION

The nature of recirculation convection over asymmetrical definite discrete heated ribs ($L_1/W = 0.51$, $L_2/W = 1.47$) in channels with the existence of both opposing/assisting flows, respectively, is investigated in the range $1.43 \times 10^5 < Ra_W'' < 1.40 \times 10^6$ to broaden our basic understanding of this type of convective heat transfer. The most significant contributions of the present study are as follows.

(1) Systematic experimental data for the local steady state natural convection heat transfer in such geometric configurations were obtained and a quantitative heat transfer correlation was established.

(2) Through flow visualization, the photographs, qualitatively, indicate that the existence of protruding ribs changes the flow characteristics and originates the recirculation zone as well as the turbulence zone in the vicinity of the rib.

(3) The heat transfer data (using laser holographic interferometry and thermocouple temperature measurement) and the flow visualization photographs suggest that the stratification and flow separation/recirculation are the major two factors influencing the temperature of the heated ribs.

(4) Based on the analyses of the photographs and interferograms, it is found that the turbulent flow should be expected in channel A when $1.29 \times 10^7 < Ra_y^* < 2.55 \times 10^9$; while, in channel B, turbulent flow should also be expected in the range of $4.92 \times 10^8 < Ra_y^* < 9.43 \times 10^9$.

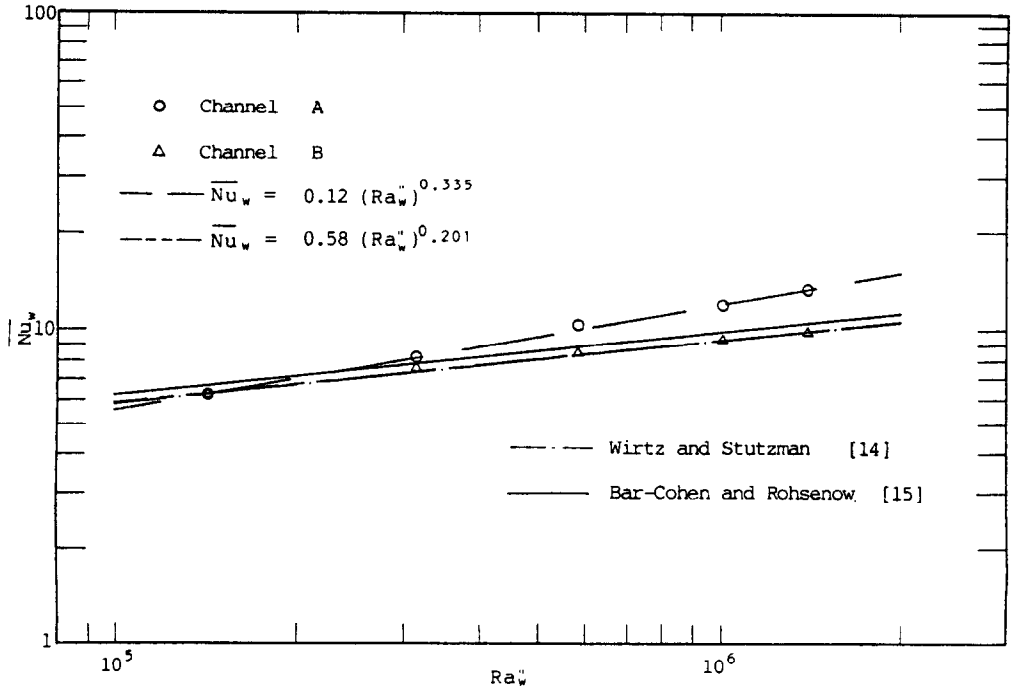

FIG. 11. Plot of average Nusselt number against modified channel Rayleigh number.

(5) Following remark (4), the average heat transfer data in channel A were correlated with a nearly 1/3 power dependence indicating a turbulent type flow whereas in channel B the data approximately exhibits a 1/5 power dependence instead.

(6) The results indicate that the Nusselt number Nu_y for the discrete heating with protrusion for both opposing/assisting flows is higher than that of a fully heated vertical channel under certain values of Ra_y^* ($Ra_y^* > 3.21 \times 10^5$). For the present range of Ra''_w, $\overline{Nu}_w$ is almost the same as that reported by Wirtz and Stutzman [14] for channel B (assisting flow) and is from 4.9 to 28.2% higher than that reported by Bar-Cohen and Rohsenow [15] for channel A (opposing flow) when $Ra''_w > 2.2 \times 10^5$.

Acknowledgement—The authors would like to thank National Science Council (NSC), Taiwan, Republic of China, for financial support under Grant No. NSC77-0401-E110-07.

REFERENCES

1. A. E. Zinnes, The coupling of conduction with laminar natural convection from a vertical flat plate with arbitrary surface heating, *J. Heat Transfer* **92**, 528–535 (1970).
2. V. P. Carey and J. C. Mollendorf, The temperature field above a concentrated heat source on a vertical adiabatic surface, *Int. J. Heat Mass Transfer* **20**, 1059–1067 (1977).
3. K. A. Park and A. E. Bergles, Natural convection heat transfer characteristics of simulated microelectronic chips, *J. Heat Transfer* **109**, 90–96 (1987).
4. R. J. Moffat and A. Ortega, Buoyancy induced forced convection. In *Heat Transfer in Electronic Equipment*, ASME HTD-Vol. 57, pp. 135–144 (1986).
5. M. D. Kelleher, R. H. Knock and K. T. Yang, Laminar natural convection in a rectangular enclosure due to a heated protrusion on one vertical wall—Part I: experimental investigation, *Proc. 2nd ASME/JSME Thermal Engng Joint Conf.*, Honolulu, Hawaii, Vol. 2, pp. 169–177 (1987).
6. J. J. Lee, K. V. Liu, K. T. Yang and M. D. Kelleher, Laminar natural convection in a rectangular enclosure due to a heated protrusion on one vertical wall—Part II: numerical simulation, *Proc. 2nd ASME/JSME Thermal Engng Joint Conf.*, Honolulu, Hawaii, Vol. 2, pp. 179–185 (1987).
7. K. V. Liu, K. T. Yang and M. D. Kelleher, Three-dimensional natural convection cooling of an array of heated protrusions in an enclosure filled with a dielectric fluid, *Proc. Int. Symp. on Cooling Technology for Electronic Equipment*, Honolulu, Hawaii, pp. 486–497 (1987).
8. M. Keyhani, V. Prasad and R. Cox, An experimental study of natural convection in a vertical cavity with discrete heat source, *J. Heat Transfer* **110**, 616–624 (1988).
9. W. Aung and R. O'Regan, Precise measurement of heat transfer using holographic interferometry, *Rev. Scient. Instrum.* **42**, 1755–1758 (1971).
10. R. Siegel and J. R. Howell, *Thermal Radiation Heat Transfer*, 2nd Edn. McGraw-Hill, New York (1981).
11. S. Shakerin, M. Bohn and R. I. Loehrke, Natural convection in an enclosure with discrete roughness elements on a vertical heated wall, *Int. J. Heat Mass Transfer* **31**, 1423–1430 (1988).
12. I. G. Choi and S. A. Korpera, Stability of the conduction regime of natural convection in a tall vertical annulus, *J. Fluid Mech.* **99**(4), 725–738 (1980).
13. G. C. Vliet, Natural convection local heat transfer on constant heat-flux inclined surfaces, *J. Heat Transfer* **91**, 511–516 (1969).
14. R. A. Wirtz and R. J. Stutzman, Experiments on free convection between vertical plates with symmetric heating, *J. Heat Transfer* **104**, 501–507 (1982).
15. A. Bar-Cohen and W. M. Rohsenow, Thermally optimum spacing on vertical natural convection cooled parallel plates, *J. Heat Transfer* **106**, 116–123 (1984).

CONVECTION NATURELLE AVEC ECOULEMENT EN OPPOSITION OU EN AIDE DANS DES CANAUX VERTICAUX AVEC DES NERVURES CHAUFFEES ASYMETRIQUES

Résumé—Une visualisation qualitative, une interférométrie holographique laser et une mesure quantitative de température sont présentées pour la convection naturelle de couches d'air dans des canaux verticaux (canaux A et B) avec des nervures chauffées asymétriques, un écoulement en opposition dans le canal A ou en aide dans B. A partir des analyses des photographies et des interférogrammes, on suggère que l'écoulement turbulent peut être atteint quand le nombre de Rayleigh local modifié est dans le domaine $1{,}29 \times 10^7$–$9{,}43 \times 10^9$ pour les deux canaux. Les données thermiques et les visualisations montrent que la géométrie considérée et la stratification sont deux raisons majeures qui influencent la température des nervures chaudes. Le nombre de Nusselt global est

$$\overline{Nu}_W = 0{,}12(Ra''_W)^{0.335}$$
$$\overline{Nu}_W = 0{,}58(Ra''_W)^{0.201}, \quad 1{,}43 \times 10^5 < Ra''_W < 1{,}40 \times 10^6$$

respectivement pour les canaux A et B. Les puissances indiquent que l'écoulement est du type turbulent dans A et du type laminaire dans B.

NATÜRLICHE KONVEKTION BEI ABWÄRTS- UND AUFWÄRTSGERICHTETER STRÖMUNG IN SENKRECHTEN KANÄLEN MIT ASYMMETRISCH BEHEIZTEN RIPPEN

Zusammenfassung—Die natürliche Konvektion von Luftschichten in senkrechten Kanälen (A und B) mit asymmetrisch beheizten Rippen wird einerseits qualitativ durch Sichtbarmachung der Strömung wie auch durch holografische Interferometrie mit Laser untersucht, andererseits quantitativ durch Temperaturmessungen. Die abwärtsgerichtete Strömung befindet sich im Kanal A, die aufwärtsgerichtete im Kanal B. Aufgrund der Analyse der Fotografien und Interferogramme wird vorgeschlagen, daß in beiden Kanälen turbulente Strömung erwartet werden darf, wenn die örtliche modifizierte Rayleigh-Zahl im Bereich von $1{,}29 \times 10^7$ bis $9{,}43 \times 10^9$ liegt. Die Meßergebnisse für den Wärmeübergang sowie die Fotografien von der Sichtbarmachung der Strömung zeigen, daß die vorgestellte Rippengeometrie und die Schichtung ganz wesentlichen Einfluß auf die Temperatur der beheizten Rippen haben. Für die Kanäle A bzw. B ergeben sich folgende Korrelationen für die mittlere Nusselt-Zahl:

$$\overline{Nu}_W = 0{,}12(Ra''_W)^{0.335}$$
$$\overline{Nu}_W = 0{,}58(Ra''_W)^{0.201} \quad 1{,}43 \times 10^5 < Ra''_W < 1{,}40 \times 10^6.$$

Die Exponenten in diesen Gleichungen zeigen, daß die Strömung in Kanal A turbulent ist, diejenige in Kanal B laminar.

ЕСТЕСТВЕННАЯ КОНВЕКЦИЯ ПРИ ТЕЧЕНИИ ВСТРЕЧНЫХ И СПУТНЫХ ПОТОКОВ В ВЕРТИКАЛЬНЫХ КАНАЛАХ С АСИММЕТРИЧНО РАСПОЛОЖЕННЫМИ НАГРЕВАЕМЫМИ РЕБРАМИ

Аннотация—Приводятся качественные результаты визуализации потока и лазерной голографической интерферометрии, а также количественные измерения температуры при естественной конвекции воздушных слоев в вертикальных каналах (каналы А и В) с асимметрично расположенными нагреваемыми ребрами, причем противоположное подъемным силам течение происходит в канале А, а спутное—в канале В. На основе анализа фотографий и интерферограмм можно полагать, что течение будет турбулентным при локальных подифицированных числах Рэлея в диапазоне $1{,}29 \times 10^7$–$9{,}43 \times 10^9$ в обоих каналах. Данные по теплопереносу и фотографии, полученные при визуализации потока, указывают на то, что геометрия ребер и стратификация являются двумя основными факторами, от которых зависит температура нагреваемых ребер. Обобщенная зависимость для среднего числа Нуссельта представлена в виде:

$$\overline{Nu}_W = 0{,}12(Ra''_W)^{0.335}$$
$$\overline{Nu}_W = 0{,}58(Ra''_W)^{0.201}, \quad 1{,}43 \times 10^5 < Ra''_W < 1{,}40 \times 10^6$$

соответственно для каналов А и В. Характер степенной зависимости свидетельствует о том, что в канале А течение является турбулентным, а в канале В—ламинарным.